Microwave properties of Ni-based ferromagnetic inverse opals

M. Kostylev,[1] A. A. Stashkevich,[2] Y. Roussigné,[2] N. A. Grigoryeva,[3] A. A. Mistonov,[3] D. Menzel,[4] N. A. Sapoletova,[5]
K. S. Napolskii,[5] A. A. Eliseev,[5] A. V. Lukashin,[5] S. V. Grigoriev,[3,6] and S. N. Samarin[1]

[1]*School of Physics M013, University of Western Australia, Crawley, 6009 WA, Australia*
[2]*LSPM CNRS (UPR 3407), Université Paris 13, Sorbonne Paris Cité, 93430, France*
[3]*Saint Petersburg State University, 199034, Saint Petersburg, Russia*
[4]*Institute of Condensed Matter Physics, 308108 Braunschweig, Germany*
[5]*Lomonosov Moscow State University, 119992 Moscow, Russia*
[6]*Petersburg Nuclear Physics Institute, Gatchina, 188300 St. Petersburg, Russia*

Investigations of microwave properties of Ni-based inverse ferromagnetic opal-like film with the [111] axis of the fcc structure along the normal direction to the film have been carried out in the 2–18 GHz frequency band. We observed multiple spin wave resonances for the magnetic field applied perpendicular to the film, i.e., along the [111] axis of this artificial crystal. For the field applied in the film plane, a broad band of microwave absorption is observed, which does not contain a fine structure. The field ranges of the responses observed are quite different for these two magnetization directions. This suggests a collective magnetic ground state or shape anisotropy and collective microwave dynamics for this foam-like material. This result is in agreement with SQUID measurements of hysteresis loops for the material. Two different models for this collective behavior are suggested that satisfactorily explain the major experimental results.

I. INTRODUCTION

Rapid progress in photonics, exploiting unusual wave properties of optical waves in structures with a submicron periodic modulation of the refractive index, has lead to creation of a new type of material known as photonic crystals.[1,2] The latter demonstrate such prominent features as Brillouin zones (BZ), the emergence of which is accompanied by a number of unique peculiarities in wave behavior, typically occurring in the vicinity of BZ boundaries, which include photonic band gaps, slow light propagation, and negative dispersion.

Naturally, the impressive achievements in photonics have inspired similar research efforts in neighboring areas of wave physics, in general, and in magnetism, in particular. Microwave properties of ferromagnetic materials are due to the temporal evolution of the magnetization vector $\vec{M}$. The latter is described by the Landau–Lifschitz equation wherein symmetry predetermines the character of the motion of $\vec{M}$ as a small-angle (for the linear regime) precession around the direction of its equilibrium.[3] The phenomenon, known as ferromagnetic resonance (FMR), describes the interaction of a microwave field with the matter. Two more physical phenomena are involved if one considers the spatial evolution of the dynamic component of magnetization at microwave frequencies: long-range dipole–dipole interactions (DDI) and the short-range exchange interaction. Thus, magnetic dynamics and consequently microwave properties of ferromagnetic materials manifest themselves through magnetic excitations propagating in the bulk of such materials known as dipole-exchange spin waves (SW). The latter, also known as magnons, are characterized by a very pronounced dispersion $\omega(K)$ (where ω is the temporal frequency, and K is the spatial frequency or the wave number) due to both temporal (via the FMR) and spatial (via the exchange interaction) dependence of the elements of the tensor of microwave magnetic permeability $\mu(\omega, K)$.

The universal nature of wave physics in periodic media dictates striking analogies between photonics and magnonics.[4] In the case of magnonics, spin waves in periodic ferromagnetic structures (magnonic crystals) are exploited.[4–13] In contrast to the photonic modes, however, in the case of magnonic crystals, the effects due to patterning of continuous magnetic films are superimposed on those already existent in its absence, such as pronounced dispersion $\omega(K)$.[14–16] Another important peculiarity of magnetic dynamics in periodically nanopatterned planar geometry is the strong uniaxial anisotropy of dispersion[16] imposed by the application of the static magnetic field in the plane of the nanostructure. This anisotropy originates from the nonuniformity of the ground state of magnetization due to static demagnetization.[17]

Artificial opals are ideally suited for applications as both photonic and magnonic crystals. While there exists extensive literature dedicated to studies of three-dimensional (3D) photonic effects in direct opals (see, for example, Ref. 18 and references therein), wave processes in inverse opal structures are far less investigated. At the same time, the technologies involved in their fabrication allow creation of 3D periodic ferromagnetic structures, which makes them extremely promising as 3D magnonic materials.

In this work, we study microwave magnetic dynamics in the inverse opals fabricated using a colloidal crystal film. This fabrication method is a 3D counterpart of the "natural-lithography" technique previously used to fabricate 2D periodic arrays of *magnetic* nanodots.[19–21] The collective magnetic dynamics in the inverse opals is studied here in the same way as in Refs. 20 and 21: using the microstrip-based applied-field resolved broadband FMR method. We also perform superconducting quantum interference device (SQUID) measurements of the hysteresis loops of magnetization for the material in order to relate the FMR resonance fields we observe to the ground state of magnetization. X-ray diffraction characterization is also carried out in order

to establish the crystallographic structure of this artificial crystal.

The paper is organized as follows: In the next section, we give details of the sample preparation and characterization; in Sec. III, we describe the experimental techniques used to perform measurements and show the results of the experiments. In Sec. IV, we discuss the experimental findings and suggest two simple theories to explain the obtained FMR data. Both theoretical models are in agreement with the experiment. It is impossible to conclude which of them is closer to reality. Given the complexity of this geometry, only micromagnetic simulations will be able to deliver an answer to this question. This modeling remains out of scope of this paper, since, for the same reason of complexity of the medium, it is hardly possible to complete such numerical modeling within a reasonable amount of time.

II. SAMPLE PREPARATION AND CHARACTERIZATION

A nickel inverse opal (IO) sample was fabricated by using electrodeposition techniques and utilizing a colloidal crystal film as a template.[22,23] The colloidal crystal film was prepared by an electric-field-assisted vertical deposition of monodisperse polystyrene microspheres (diameter $D = 530$ nm; radius standard deviation $< 10\%$) onto a Si(100) wafer coated with a 100-nm-thick gold layer.[24] The electrodeposition of nickel was carried out in a three-electrode cell from aerated 0.6 M $NiSO_4$ + 0.1 M $NiCl_2$ + 0.3 M H_3BO_3 + 3.5 M C_2H_5OH electrolyte at -0.9 V versus Ag/AgCl reference electrode at room temperature. The area of the sample was 0.6 cm^2. In order to obtain the free-standing metallic structure on the substrate, the polystyrene microspheres were dissolved by placing the sample in toluene for several hours. According to scanning electron microscope (SEM) imaging, the inverse opal consists of 11 layers, which is in good agreement with the number of oscillations on current transient recorded during the electrodeposition. The total thickness of the film is 4.76 μm.

III. EXPERIMENT

Before starting microwave measurements, we carried out structural and static characterization of the Ni inverse opal. SEM images, providing information about quality and major structural features of the sample, were recorded by a LEO Supra 50 VP instrument. According to the results of SEM [Fig. 1(a)], the average center-to-center distances between spherical voids are 515 ± 10 nm. From the top view, one sees that the sample is actually a "patchwork"-type film: It is characterized by ordered domains separated by cracks [Fig. 1(a), lower panel]. These "patches" are relatively large (typical domain size is 20–200 μm^2) and only slightly misoriented with respect to each other. At the same time, ordering within each "patch" is practically perfect [Fig. 1(a), upper panel].

The structural studies of the Ni inverse opal (Ni IO) were performed with high-resolution x-ray diffraction using the compound refractive optics.[24] This method was successfully used to investigate different stacking sequences in opal-like structures based on polystyrene, or silicon oxide spheres,[24,25] and of inverse opals based on various oxide materials (TiO_2, SiO_2, and Fe_2O_3).[26,27] The measurements were taken at
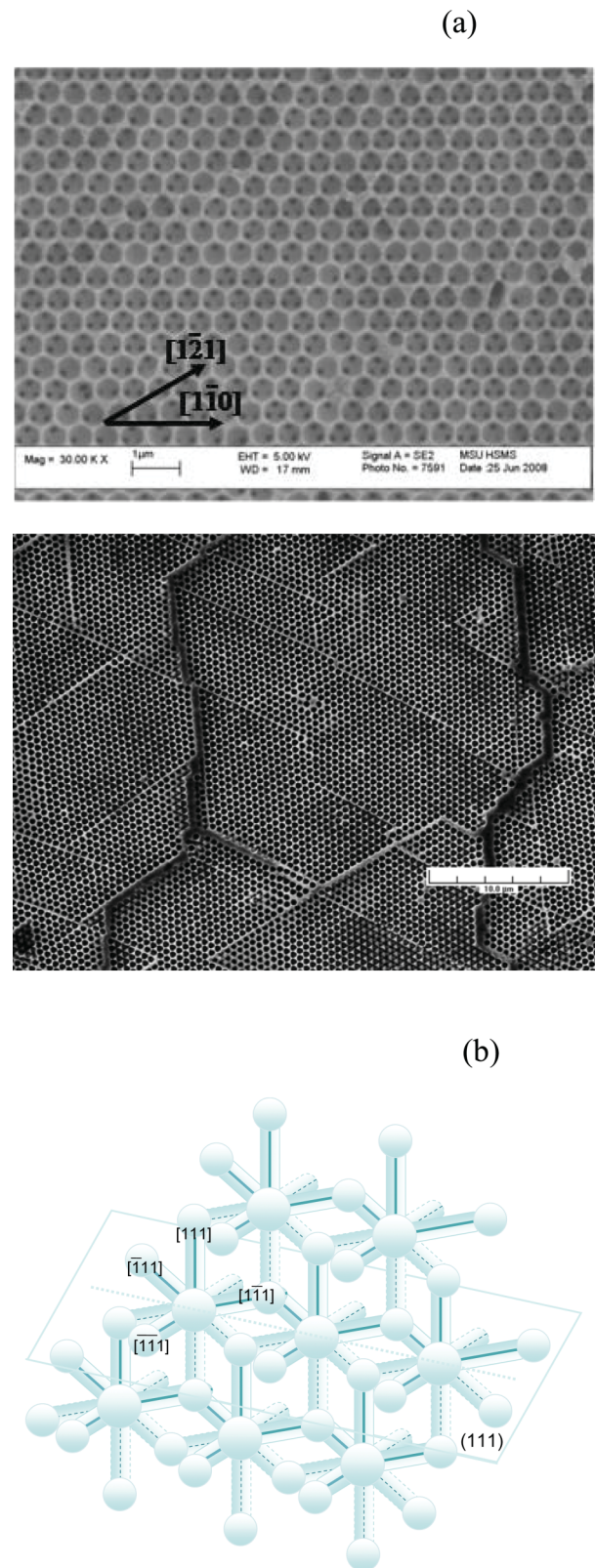

(a)

(b)

FIG. 1. (Color online) (a) Top view SEM images of the nickel inverse opal. The arrows indicate two prominent crystallographic axes [1$\bar{1}$0] and [1$\bar{2}$1], which lie in the film plane; and (b) crystallographic structure of the inverse opal. In (b): larger "spheres" denote the positions of the centers of cubic (C) basic elements, and the smaller spheres denote ones for the nanotetrahedrons. (Do not confuse these spheres with the real spherical voids!)

DUBBLE BM26 line at the European Synchrotron Radiation Facility (Grenoble, France). The details on the experimental setup are given in Refs. 28–30. Briefly, diffraction of a monochromatic 13 keV x-ray beam ($\lambda = 0.095$ nm; $\Delta\lambda/\lambda = 2 \times 10^{-4}$) was registered behind the sample at a distance of 8 m by a 2D charge-coupled device (CCD) detector (Photonic Science) with 4008×2671 pixels of 22.7 μm $\times$ 22.7 μm. In order to achieve angular resolution needed to study these large-period structures, the beam was focused at the detector by a set of compound refractive lenses.[31] The diameter of the x-ray beam was about 0.5 mm. Figures 2(a)–2(c) show the diffraction patterns for the reciprocal lattice of the face-centered cubic (fcc) structure cut by the (111), (101), and (010) planes, respectively. Most of the Bragg peaks correspond to the fcc structure [indexed in the panels (d), (e), and (f)]. Additional reflections in panels (a), (b), and (c) can be attributed to either finite thickness of the crystal or stacking disorder as well as to other types of disorder.[32] The few stacking faults run along the $\langle 111 \rangle$ axes.[24]

In general, a self-assembled artificial-opal template is composed of close-packed layers. The layers can form different structures depending on their stacking sequence: a fcc structure (ABCABC...), a hexagonal close-packed (hcp) structure (ABABAB...), as well as a random hexagonal close-packed (rhcp) structure, for which the close-packed layers are arranged in random fashion.[33] It was theoretically found that there exists thermodynamic preference of the fcc structure over the hcp one due to a tiny entropy difference between these two structures.[34] This finding is supported by numerous experimental results of preferable crystallization of colloidal particles with fcc order (see, for instance, Refs. 35 and 36). Typical colloidal crystals, however, are composed of fcc fragments separated by stacking faults or hcp fragments.[35,37,38] The inverse opallike structure [Fig. 1(b)] fully duplicates the 3D net of voids of the artificial-opal template used to synthesize the sample with the electrochemical method. Details of the investigation of IO imperfections are given in a number of papers.[24–27,39,40]

One can consider IO as an assembly of small metallic particles duplicating the shape of the voids between the spheres and connected to each other via thin (several tens of nanometers) and long (several hundreds of nanometers) cross pieces. Hence, the voids of the artificial opal have quasicubic and quasitetrahedral shapes with concave surfaces. Individual voids are interconnected by vertices and, after filling the voids in, a lace free-standing opal-like structure emerges. The basic element of such a structure is the chain quasitetrahedron–quasicube–quasitetrahedron (T-C-T). These chains run along the $\langle 111 \rangle$ directions. The complete structure is obtained by translating the basic element and placing it in the positions of the fcc structure. Thus, it is clear that the resulting structure is able to impose spatial periodicity and preferred magnetization directions along certain crystallographic axes of IO.[24]

There are a number of prominent crystallographic directions in the structure of IO. The aforementioned axes $\langle 111 \rangle$ are the first of them [Fig. 1(b)]. One of these axes is perpendicular to the film surface, and there also three axes at angles of 70 degrees to the normal. Along these directions, each sequence of the three elements is separated by a void (V) left by the removal of a polystyrene sphere, such that the complete unit cell along $\langle 111 \rangle$ is T-C-T-V. One sees that the Ni chains are not continuous; they represent "dashed" lines formed by the metallic objects T-C-T, which are 850 nm long, have a mean diameter of 90 nm, and are separated from each other by 750-nm-wide gaps (V). There are also chains of the type V-T-C. They run along the directions $\langle 121 \rangle$. The respective metal objects (T-C) are 560 nm long and are separated by 530-nm-wide gaps (V). There are three of these directions in the sample plane [Fig. 1(a), upper panel], and three at the angle of 19.5 degrees to the film normal.

The last prominent directions on IO lattice are the directions $\langle 110 \rangle$. Importantly, the metal chains in these directions are continuous and lie in the film plane (there are six of them in this plane). However, these chains are not straight: They represent zigzags with a characteristic angle of the zigzag line of 120 degrees [Fig. 1(a), upper panel].

The dynamic properties of the Ni IO are studied with the FMR method in the 2–18 GHz frequency range. We also run SQUID hysteresis loops for the material to shed light
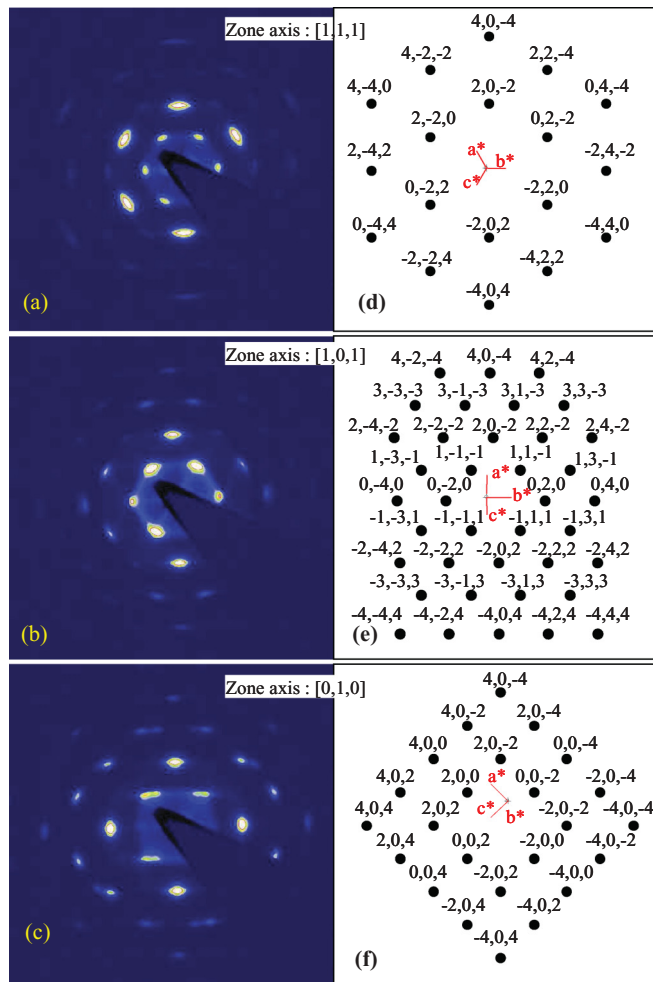

FIG. 2. (Color online) (a)–(c) Microradian x-ray diffraction patterns for the reciprocal lattice of the fcc structure cut by the (111), (101), and (010) planes, respectively. (d)–(f) Sets of Bragg reflections of the fcc structure in the experimental geometries corresponding to diffraction patterns (a)–(c). Note that this experiment was performed on a different, but very similar IO crystal with the average center-to-center distances between spherical voids: 730 ± 10 nm.

on the ground state of magnetization for the material. The characterization of the ground state is carried out at 300 K using a Quantum Design MPMS-5S SQUID magnetometer. In SQUID measurements, the samples are oriented with the film plane parallel to the magnetic field **H** ($\theta = 90°$, in-plane), i.e., with [111] axis perpendicular to **H**, or with the film plane perpendicular to **H** ($\theta = 0$, out-of-plane), i.e., with [111] axis parallel to **H**, or at an angle θ ranging from 0° to 90° with respect to the field **H**. Rotation is around the [20$\bar{2}$] axis of IO structure.

In our broadband FMR experiments, we use a section of a 1.5-mm-wide microstrip line to drive magnetization precession. Microwave absorption spectra are measured at a number of fixed frequencies ranging from 2 to 18 GHz, while sweeping the magnetic field **H** from -8000 to 8000 Oe. The measurements are run at room temperature. We use the field-modulated FMR method; the frequency of the modulating field that is parallel to **H** is 220 Hz, and its amplitude is 8 Oe. The output of the microstrip line is connected to a microwave diode. The rectified signal from the output of the diode is applied to the input of a digital lock-in amplifier locked to the same frequency of 220 Hz. In this arrangement, the signal from the digital output of the lock-in is proportional to the first derivative of the signal of FMR absorption with respect to the applied field ("differential absorption").

Similar to the case of static measurements, in our dynamic experiments we employ two principal geometries: (i) the magnetic field **H** is applied in the plane of the film (the in-plane case), and (ii) the field **H** is applied normal to the film plane (the out-of-plane case). The exemplary raw experimental results are presented in Fig. 3. The differential absorption is plotted as a function of the applied field for two directions of the applied field: in-plane ($\theta = 90°$) and out-of-plane ($\theta = 0$) in panels (a), (b), and (d). In panel (c), we also plot an example of the first antiderivative of these raw data ("absorption traces") in the same graph. This example is shown because this is a more conventional form for the presentation of the raw broadband FMR data and is natural for the widely used microwave vector network analyzer FMR.[41] As one sees from the absorption trace, microwave power is absorbed in a wide range of applied fields for each given driving frequency. Also from the comparison of these two raw data presentations, one clearly sees that the field modulation or differential absorption method allows one to resolve the fine structure of the absorption peaks, which is almost lost in absorption (i.e., antiderivative) traces. This clearly demonstrates the advantage of the field-modulation FMR method with respect to the microwave vector network analyzer method.[41] The presence of the fine structure in the out-of-plane data suggests that the broad absorption peaks seen in the in-plane FMR data in Fig. 3 are absorption zones consisting of a number of weakly resolved resonances rather than a single resonance mode.

The results of processing the raw FMR data from Fig. 3 are summarized in Fig. 4. The points in Fig. 4 correspond to the peaks observed experimentally. The data are plotted as the resonant frequency f vs the respective resonant magnetic field **H**. Since for the in-plane FMR no fine structure is resolved (Fig. 3), we just plot the position of the maximum of the respective absorption (antiderivative) curves [Fig. 4(a)]. In the respective out-of-plane FMR summary graph [Fig. 4(b)], we
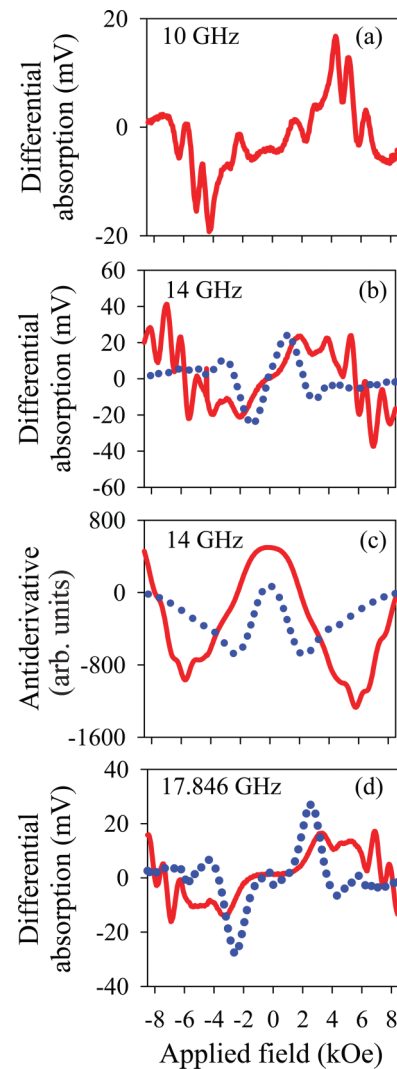
FIG. 3. (Color online) Raw FMR data. (a), (b), and (d): Amplitude of the differential absorption vs applied field. (c) Antiderivative of the data in panel (b). Solid curves: data for the out-of-plane magnetization direction. Dotted lines: data for the in-plane sample magnetization. The frequencies at which the data were taken are indicated in the panels.

plot the positions of mid-distances between a maximum in a *differential* absorption curve and the nearest minimum located from the higher-field side of the respective maximum.

In the same graphs, we also place the sections of the respective hysteresis loops. The insets to Figs. 4(a) and 4(b) show the complete hysteresis loops. From the comparison of the SQUID and FMR data, one finds that in the range of frequencies accessible with our FMR setup, the FMR response exists near the saturating field for the IO.

Note that both FMR and SQUID in-plane data have been taken for a number of applied field directions in the IO plane. No dependence of magnetic properties of IO on the direction of the applied field in the film plane has been found in these measurements. However, as seen from Fig. 4, both methods demonstrate strong dependence of magnetic properties on the out-of-plane angle θ.
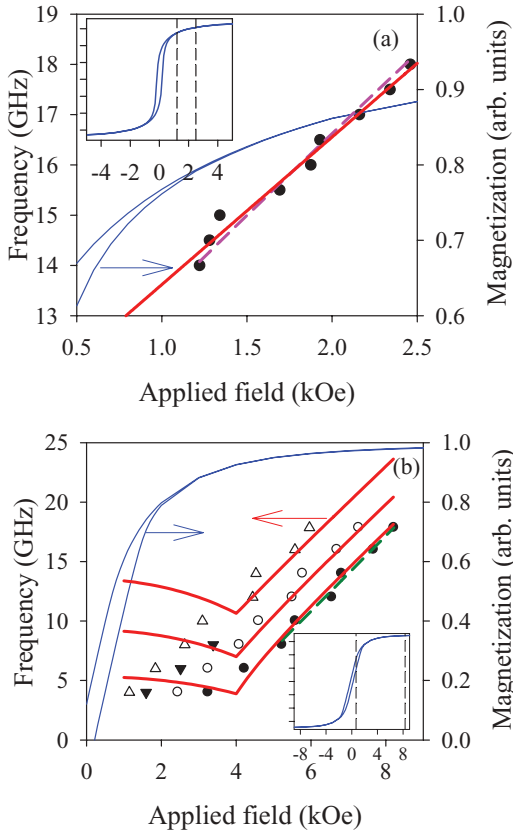
FIG. 4. (Color online) FMR frequencies vs resonance fields and hysteresis loops taken with SQUID. (a) In-plane sample magnetization ($\theta = 90°$). (b): Out-of-plane sample magnetization ($\theta = 0$). Dots: experimental FMR data. Filled circular dots correspond to the mode that we assume to be fundamental in both theories. Other symbols then correspond to higher-order modes. The mode shown by the filled triangles possibly originates from splitting of the mode shown by the open triangles in two modes at small applied fields where sample is not fully saturated. Dashed fines: fits of the FMR data with the theory of the effective continuous film. Thick solid lines: fits with the theory of effective cylinders. Thin solid lines: respective parts of the hysteresis loops. Insets: complete hysteresis loops.

In addition, out-of-plane FMR measurements have been taken on a continuous reference film grown with the same electrodeposition method. From the obtained measurement results, a value of the effective saturation magnetization of 5 kOe has been extracted. This value can be interpreted as a sum of the standard saturation magnetization for nickel $4\pi M_s = 6$ kG and of an effective field of normal uniaxial anisotropy of 1 kOe. From the literature,[42] it is known that in nickel films, if they are highly mechanically stressed, a significant normal uniaxial anisotropy can be induced through magnetostriction. The presence of such anisotropy is also consistent with results of in-plane FMR measurements, which have also been taken on this sample.

IV. DISCUSSION

The form of the basic element of the IO periodic structure is far from ellipsoidal, and hence the distribution of the static magnetization within it is highly nonuniform. More

specifically, it can be regarded as a 3D chain of SW resonators localized in the zones of pronounced inhomogeneities of the static magnetization, known also as "SW quantum wells."[43] Much will depend on the size of such "quantum wells," distances between them, and the relative orientation, and thus on the strength of the dipolar and exchange coupling between standing SW modes localized in such resonators. To estimate it, knowledge of profiles of static magnetizations is required. If dipolar coupling between these resonators is strong, dynamic behavior is explained in terms of collective Bloch spin-wave modes. The fine structure in Fig. 3 observed for the out-of-plane magnetization of IO is then the FMR responses of a number of collective modes that differ by localization of magnetic dynamics on the chains oriented at specific angles to the applied fields, on particular elements on the chains (quasitetrahedron or quasicube), and on particular areas (wells) inside the elements. The collective dynamic stray field of precessing magnetization locks phases of precession in individual elements of the same type, which produces a particular collective mode.

On the contrary, if this coupling is weak, no collective dynamics will be detectable. In this case, the fine structure in Fig. 3 observed for the out-of-plane magnetization of IO is just a discrete spectrum of eigen-frequencies of individual 3D spin-wave resonators of different types. In order to understand what kind of dynamics the IO under study supports—collective or individual—extensive and, unfortunately, extremely time-consuming, numerical simulations are needed. Conducting them is out of scope of the present paper. Instead, we make use of two different approximate models, both based on the results of the static and crystallographic characterizations of the material (see the discussion in Sec. II). The first model assumes strong coupling of *all* individual T and C resonators such that the material behaves as an effective continuous film. The second approach assumes that the dynamic coupling is small and anisotropic such that the FMR response originates from dynamics of individual linear chains of basic elements constituting the crystal.

The previous discussion suggests that knowledge of the ground state of magnetization is important for correctly explaining the magnetic dynamics. Analysis of the hysteresis loops for the material may provide some understanding of the ground state. The SQUID measurements (Fig. 4) have shown that a quasirectangular shape of the hysteresis loops observed for $\theta = 90°$ (in-plane case) is typical for magnetizing a magnetic sample along an easy axis. This shape is gradually transformed into a less rectangular and noticeably inclined one, suggesting a hard magnetization direction for the out-of-plane case. Comparison of $M(H)$-dependences at different θ reveals not only a reduction in M_R/M (M_R is magnetic remanence), but also a change in the coercive field from $H_C = 200$ Oe for $\theta = 0$ to 160 Oe for $\theta = 90°$ with a maximum at $H_C = 213$ Oe for $\theta \approx 30°$ (not shown). This suggests a transition from incoherent rotation (curling) to coherent rotation when the applied field rotates from the easy axis (in the film plane) to the hard magnetic axis (perpendicular to the film plane). The first mechanism is typical for the processes of magnetization switching in materials with pronounced shape anisotropy, or the shape anisotropy of single-domain particles.[44] Magnetization reversal in materials with large

magnetocrystalline anisotropy[45,46] proceeds via the second mechanism.

A. Model of the effective continuous film

Often it is possible to describe a collective motion on a periodic array using an effective continuous-medium approximation. In this case, one introduces effective demagnetizing factors for the array, which reflect both demagnetizing fields of individual elements and the collective dipole field of the array. For the simplest quasi-1D case of arrays of parallel dipole coupled stripes magnetized along the longitudinal direction, this was recently shown theoretically in Refs. [47] and [48], and for the similar case of arrays of nanocylinders in Refs. [49] and [50]. The same obviously applies to higher dimensions.

To describe magnetic dynamics for the medium, the Kittel equation is used, and the effective demagnetizing coefficients for the medium are extracted from the experimental data. Depending on the characteristic size of the base elements, either only demagnetizing fields are included into Kittel equation[51,52] or both dipole and exchange contributions are included.[53]

In our case, the base elements are of sizes for which both dipole and inhomogeneous exchange fields are important. Furthermore, our material is connected across the whole volume (i.e., there is no discontinuity within the Ni-phase of the material: From any point inside the Ni phase one can reach any other point inside the metal by taking a path that does not leave the metal phase). Therefore, one may also expect a collective inhomogeneous dynamic exchange field for this material that originates from the nonuniformity of dynamic magnetization on the length scale given by the sample thickness.

The absence of the in-plane angle dependence for both hysteresis loops and in-plane FMR data, and also the fact that the in-plane FMR frequencies are considerably larger than the out-of-plane ones for the same values of the applied field (Fig. 4) suggest that the crystal may behave as an effective continuous film, at least for these two particular magnetization directions. To check the validity of this idea, the in-plane and the out-of-plane FMR data were fitted with the respective Kittel formulas.

Since no anisotropy is seen in the in-plane angle-resolved SQUID and FMR data, it is appropriate to assume that the two in-plane demagnetizing factors N_{xx} and N_{yy} are equal ($N_{xx} = N_{yy} = N$), which implies that the out-of-plane demagnetizing factor is $1-2N$. For simplicity, we neglect the nondiagonal terms of the demagnetizing tensor, which implies that the macroshape of our object is close to one of an ellipsoid of rotation. Indeed, in the limiting case of very large packing density of base elements, the dipole coupling of individual elements should result in the behavior of the array as a continuous film, which is a particular form of an ellipsoid.

We repeat that N takes into account the collective character of the dynamic and static dipole fields of the sample.[53] We also add the effective exchange field H_{ex} for the array,[53] which we also assume isotropic for the same reason. Then, for the case of the out-of-plane magnetization, the respective Kittel

formula reads:

$$f = \gamma[H - 4\pi M_s(1 - 3N) + H_{ex}], \quad (1)$$

and for the in-plane magnetization case, it takes the form

$$f = \gamma\sqrt{(H + H_{ex})(H + 4\pi M_s(1 - 3N) + H_{ex})}. \quad (2)$$

One sees that if one treats $4\pi M_s(1 - 3N) \equiv 4\pi M$ as the effective saturation magnetization $4\pi M$, both formulas reduce to the respective Kittel formulas for a continuous film.

First we make use of Eq. (1) to fit the experimental data for the case of the perpendicular magnetization. In line with the idea of the effective film, we assume that the lowest set of frequencies [filled circles in Fig. 4(b)] originates from the "fundamental" FMR mode for the effective film. Note, that we do not specify the origin of this mode, we just assume that this mode is "fundamental," because Eq. (1) suggests that contributions of N and of H_{ex} to the frequency of this mode should be minimum from all the modes seen in Fig. 4(b). As one sees from Eq. (1), the slope of f vs H is given solely by the gyromagnetic coefficient γ. This allows one to extract the value for γ from the experimental data. We use only the experimental points for the well magnetically saturated state. The hysteresis loop in Fig. 4(b) suggests that the data obtained for $H > 5$ kOe correspond to the saturated state. Indeed, they are well fitted with a straight line (dashed line in the figure) using the least-square regression method. The value of γ we obtain from this fit is quite reasonable: 2.98 MHz/Oe. Given this value, from the point of intersect (not shown) of this straight line with the axis of frequencies, we now extract the value of $4\pi M - H_{ex} = 2993$ Oe. Substitution of both extracted parameters into Eq. (2) leaves just one parameter unknown, which is $4\pi M$. We extract the value for this parameter by fitting the experimental points in Fig. 4(a) with Eq. (2) [dashed line in Fig. 4(a)]. We obtain $4\pi M = 4.702$ kOe and $H_{ex} = 1709$ Oe. Both parameters have reasonable values, because $H_{ex} < 4\pi M$, which confirms that the mode under study is indeed "fundamental," and because $4\pi M$ is relatively close to, but smaller than, the standard value of saturation magnetization for nickel, $4\pi M_s = 6$ kOe. Furthermore, 4.702 kOe is approximately the out-of-plane saturation field for the sample, as seen from the SQUID data in Fig. 4(b), which is consistent.

From the value of $4\pi M$ and the standard value of saturation magnetization for nickel, one can also extract the effective demagnetizing factor N. One obtains $N = 0.072$, which is quite a reasonable value, if one compares it, e.g., with the effective demagnetizing factors of nanostripes (Fig. 2 in Ref. [52]). We may also try to compare the effective exchange field we obtain with one that may be expected from a continuous film of the same thickness. We use the formula $H_{ex} = 4\pi M_{(s)}\alpha k^2$, where $\alpha = 2A/(4\pi M_{(s)}^2)$, and $A = 9 \times 10^{-12}$ J/m is the exchange constant for nickel. We obtain $k = 6.7 \times 10^5$ rad/cm or 6×10^5 rad/cm, which corresponds to the half-wavelength of a standing spin wave of 46 nm or 53 nm, if we use either 6 kOe or 4.7 kOe for the saturation magnetization, respectively, in these formulas. One sees that these values are considerably smaller than the film thickness (approximately 4.76 μm) but of the same order of magnitude as the mean width (90 nm) of basic elements (see the discussion in Sec. II). Thus, in the

framework of this model, the exchange contribution to the total energy of the standing spin wave originates from the nonuniformity of the Bloch-wave profile across the individual basic elements, but it is not given by the wave number of the standing Bloch wave $n\pi/L$, where $n = 0,1,2\ldots$ (recall that $L = 4.76\ \mu$m is the film thickness).

An important question arises at this stage: Why are these higher-order modes not seen in the in-plane FMR data? There are two equally possible answers to this question that are in agreement with this model. Firstly, it is known that the higher-order exchange modes of magnetic films are often seen in the out-of-plane FMR measurements but not seen in the data taken on the same sample for the field applied in-plane (see, e.g., Ref. 54). The same applies to such nanoelements as nanodiscs.[20]

Secondly, due to a very complicated character of the magnetization dynamics on the microscopic scale, it may happen that the previous analysis can be valid only for the mode with the most in-phase precession of all spins in the material. In the analysis above, we assumed that this is the mode with the lowest frequency in Fig. 4(b), but basically it may be any of the partially resolved modes. The other modes may have quite different origins, and the effective medium approximation may not be valid for them at all. In the latter case, the fact that just one mode is seen for **H** applied in-plane suggests that the only mode seen in this case is the collective mode with the most in-phase precession of all spins, and the other modes are not excited or are degenerate in frequency with the fundamental one. Note that the value of the characteristic wavelength we extracted above from the exchange field may suggest that this second explanation may be more likely.

We conclude the description of this section by stating that it is impossible to check if this phenomenological model correctly reflects the reality. Only micromagnetic simulations may shed light on the magnetic dynamics on the mesoscopic scale. The same applies to the alternative, "more microscopic," model which we suggest in the following.

B. Model of the effective cylinders

Let us now discuss the alternative model, which assumes that the microwave dynamics originates from eigenmodes of linear chains of basic elements. We suggest that the collective motion of these chains may be approximated with dynamics of long cylinders of nanoscale cross-sections (Fig. 5). We justify this assumption by the fact that Fig. 4(a) displays a feature known as a characteristic signature of the presence of structural elements with a pronounced uniaxial anisotropy, for example, cylinders, when magnetized along the easy axis: There is no signal at low frequencies. This agrees well with the results of static characterization, which has revealed a major role played by chains of cubes and therahedrons in the magnetic behavior of IO structures.

As we stated in Sec. II, there is a number of chains of different lengths and different orientations with the respect to the film normal and its plane. Each of them may potentially contribute to the FMR response. It is impossible to find out which type of chains gives the main contribution unless one carries out micromagnetic simulations. The latter task is beyond the scope of this paper (as it has been already stated).
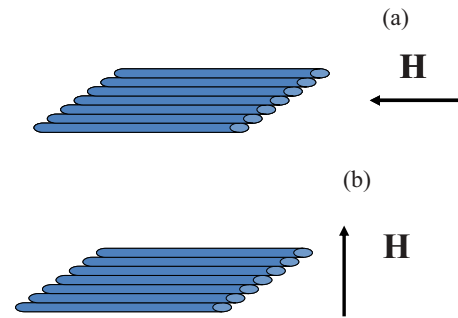

FIG. 5. (Color online) Model of effective nanocylinders. (a) The IO film is magnetized in-plane, which is along the cylinder axes of the effective cylinders. (b) The IO film is magnetized out-of-plane, i.e., perpendicular to the axes of the effective cylinders.

In the following, let us assume that the main contribution to the FMR response originates from the chains that run along the axes $\langle 111 \rangle$ and $\langle 110 \rangle$. The chains of $[1\bar{1}0]$ type are continuous and lie in the film plain. For simplicity, we neglect their zigzag character. We also assume that the "dashed lines" of complex nano-objects of type T-C-T along the axes $\langle 111 \rangle$ (see Sec. II) may be considered as chains of nanocylinders with an aspect ratio 850 nm/90 nm = 9.5 (length/diameter, respectively) with their long axes oriented along the chains. The ends of these cylinders are separated by 750-nm-long voids. This large aspect ratio of 8 may be effectively even larger due to a possible magnetostatic coupling of the cylinders along the chain. This implies that, very approximately, these chains may also be considered as effective quasiinfinite cylinders. There are four groups of these cylinders oriented along the axes $\langle 111 \rangle$ of the structure. The shortest one is oriented along the normal to the IO film plane, and the other three groups are composed of the longer chains at angles of 70 degrees. In the following, we will also assume that the FMR response originates from the longer effective cylinders, that the difference between 70 degree and the in-plane direction ($\theta = 90°$) is negligible, and that for each in-plane angle, only the chains for which the direction is the closest one to the direction of the applied field contribute to the FMR response. The large number of the cylinders of these two types ($\langle 111 \rangle$ and $\langle 110 \rangle$) oriented close to the film plane explains well the absence of any magnetic anisotropy in the film plane found in our SQUID and FMR studies.

For an infinite cylinder magnetized along its long axis [Fig. 5(a)], the dependence of the frequency of the lowest magnetostatic mode, known also as the Kittel mode, on the magnetic field is described by a very simple expression:[55]

$$f = \gamma(H + 2\pi M), \qquad (3)$$

where γ is the gyromagnetic ratio, $4\pi M$ is the saturation magnetization, and H is the applied magnetic field. The experimental points are well fitted with this straight line [the thick solid line in Fig. 4(a)]. However, this least-square regression fit gives a value for $4\pi M = 7282$ G, which is slightly greater than the value of the saturation magnetization for bulk nickel known from the literature: $4\pi M = 6000$ G. (The extracted value for γ is very close to the extracted with the theory (a): 2.9344 MHz/Oe.)

In the Appendix, we extend this model to include the dipole–dipole interactions between the effective chains. Our

estimation demonstrates that the Kittel frequency variation due to interchain DDIs does not exceed 3%, which is negligible in our case of the material with large microwave losses. Thus, it cannot explain the increased value of $4\pi M = 7282$ G that we extract from these fits.

A more plausible explanation for this discrepancy is that the form of the crystallite clusters is not exactly cylindrical, and an amendment to Eq. (3) is needed. For example, if one replaces 2 in the denominator of the second term on the right-hand side by 1.58, the conventional value of the saturation magnetization, $4\pi M = 6000$ G, can be retained.

Another contribution is also possible: Since the field inside the crystallites is highly inhomogeneous, strong localization of the oscillations originating from this field nonuniformity may result in a strong dynamic exchange effective field and push the experimental frequency upward.[44]

In Fig. 4(b), similar results for the out-of-plane case are shown. To test the adequacy of our approximation of cylindrically shaped inclusions, we calculated, as in the previous case, the frequencies of the fundamental Kittel mode, this time for the configuration with the magnetic field applied perpendicularly to the axis of the cylinder [Fig. 5(b)]. For the saturated case $H > 2\pi M$, this frequency is given by

$$f = \gamma \sqrt{H(H - 2\pi M)}. \tag{4}$$

Interestingly, similar to the in-plane case, in order to fit these data for the fundamental mode [the lowest-frequency [bottom] one in Fig. 4(b)], we have to set $4\pi M = 7282$ G. Naturally, the arguments stated in the paragraph above are equally applicable here. One sees that the agreement for the case of the saturated sample is good. Similar to the in-plane case in the Appendix, we show that inclusion of the interchain DDI does not improve accuracy of this model.

Thus, this alternative model of the effective cylinders is also able to explain our experimental data. Although being more speculative because of being based on a larger number of assumptions, it has one important advantage with respect to the model of the effective continuous film: It provides a natural explanation for the multimodal character of the FMR spectrum seen in the out-of-plane field configuration [Fig. 4(b)]. In the framework of this model, the mode frequency splitting Δf can be regarded as an important feature that characterizes the studied magnetic structure. The higher-order FMR modes of a cylinder are not spatially uniform, and it is necessary to take into account the inhomogeneous exchange interaction. According to our experimental results, Δf is of the order of approximately 3 GHz. In our estimations above, we relied on the theory initially developed for an infinite isolated cylinder elaborated in Ref. 56. We took into account the dipolar interactions between cylinders by modifying the saturating field: In our calculation, the saturating field reads $2\pi(1 + P)M$ instead of $2\pi M$; the eigen-frequencies are thus derived from the following expression: $(\omega/\gamma)^2 = (H_{\text{eff}} + D(K_{\text{n,p}})^2)(H_{\text{eff}} + D(K_{\text{n,p}})^2 + 4\pi M - 2\pi M \cos^2\theta)$, where $H_{\text{eff}} = 0$ and $\cos\theta = H_{\text{ext}}/2\pi(1 + P)M$ in the case of unsaturated cylinders, i.e., $H_{\text{ext}} < 2\pi(1 + P)M$, while $H_{\text{eff}} = H_{\text{ext}} - 2\pi(1 + P)M$ and $\cos\theta = 1$ in the case of saturated cylinders, i.e., $H_{\text{ext}} > 2\pi(1 + P)M$. The exchange constant D is $2A/M$, and the "wave numbers" $K_{\text{n,p}} = a_{np}/R$ with $a_{11} = 1.84$, $a_{12} = 3.05$,

and $a_{13} = 4.20$. Assuming the oscillation of the magnetization is uniform along the cylinder axis, each eigenmode, as in any cylindric waveguide,[57] is characterized by two indices: "n" and "p." The first one originates from radial and azimuthal profiles, expressed in terms of Bessel functions of "nth" order and $\exp(in\theta)$, respectively, while the second one is introduced to label the rank "p" of the corresponding radial solution for given boundary conditions.[56,58] The symmetry of the azimuthal modes prohibits their excitation by a spatially uniform microwave field of the FMR setup. Hence, the higher-order modes in Fig. 4(b) are higher-order radial modes. Our calculations, performed with the exchange constant $A = 0.9 \times 10^{-6}$ erg/cm and $4\pi M = 7282$ G, show that the frequency splitting $\Delta f \approx 3$ GHz for lower radial modes ($n = 1$, $p = 1,2,3$) is best fitted if the effective cylinder radius is set at $R = 35$ nm, which is of the same order of magnitude as the size of the basic element [see Fig. 4(b)].

V. CONCLUSIONS

In this work, we have carried out experimental studies of the broadband FMR response of an inverse opal made from nickel. Our investigation revealed a broad band of frequencies and fields in which resonant absorption takes place. For the out-of-plane direction of magnetization, a number of partially resolved modes is observed. For the in-plane sample magnetization, individual modes are not resolved: One observes a wide band of absorption.

Resonance frequencies are quite different for these two magnetization directions, which suggests dynamics of collective type and a collective magnetic ground state (shape anisotropy) originating from the dipole–dipole interactions. The performed SQUID measurements of hysteresis loops of magnetization confirm this conclusion. Two different phenomenological models we suggest are in agreement with our experimental data. One of these models treats the sample as an effective continuous film. The second considers it as a set of uncoupled nanocylinders oriented in the film plane. It is impossible to judge which of these models is closer to reality. Complicated micromagnetic simulations are required to confirm or reject either of these theories.

APPENDIX: THE ROLE OF THE DIPOLE–DIPOLE INTERACTIONS IN THE EFFECTIVE CYLINDER MODEL

First, it should be noted that in composite materials, DDIs between ferromagnetic inclusions lead to a shift in the effective resonance frequencies of the SW modes, including the lowest Kittel one.[49] To estimate the role of this mechanism, we have employed a simple and physically sound effective magnetic

anisotropy approach proposed in Ref. 49. It has proved to be valid for composite films of a specific geometry: vertical, or out-of-plane, ferromagnetic nanowires buried in an Al_2O_3 matrix and for which the concentration in the matrix is characterized by a packing density P. The wires have the shape of a cylinder. To take into account the competition between the shape anisotropy of an individual wire ($P \to 0$) and the macroshape anisotropy of the whole film sample ($P \to 1$), which is of planar type, the following formula for the resultant effective magnetic anisotropy has been proposed:

$$H_a^{\text{dip}} = H_a - 6\pi P M. \quad \text{(A1)}$$

In our case, however, the (quasi-)cylinders are oriented horizontally, or in-plane [Fig. 5(a)], which complicates the analytical analysis to some extent. However, without much difficulty, one can derive the following expressions for the Kittel frequencies for arrays of parallel cylinders of infinite length with the external magnetic field applied along the axes of the cylinders:

$$f = \gamma \sqrt{(H + (1 + P)2\pi M) \cdot (H + (1 - P)2\pi M)}. \quad \text{(A2)}$$

If $P \to 0$, which corresponds to the case of an individual wire, one recovers Eq. (3). Correspondingly, if we consider another limiting case $P \to 1$ (continuous film), Eq. (3) reduces to the expression for the frequency of the Damon–Eshbach mode in a tangentially magnetized film, $f = \gamma \sqrt{H \cdot (H + 4\pi M)}$, which confirms validity of the adopted theoretical model.

In the IO, the concentration of the ferromagnetic phase (which is the same quantity as the packing density P) is unlikely to exceed 26%. Our computations based on Eq. (A2) show that even for the case $P = 0.26$, the frequency variation due to interchain DDIs does not exceed 3%, which is negligible in our case of materials with large microwave losses. Interestingly, the frequency in the presence of DDIs is slightly decreased, which is not surprising. In any case, this physical mechanism, although important in the general case, can be excluded in our case of the sample with relatively low Ni concentration.

To estimate the contribution of intercylinder DDIs in the out-of-plane field configuration [Fig. 5(b)], we have derived the following expressions, which extend Eq. (4). For the case of incomplete saturation ($H < (1 + P)2\pi M$), we have:

$$f = \gamma \sqrt{(2\pi M)^2 - \left(\frac{H}{(1 + P)}\right)^2} \cdot \sqrt{(1 + P)}, \quad \text{(A3a)}$$

and in the saturated case ($H > (1 + P)2\pi M$), we obtain:

$$f = \gamma \sqrt{(H - P \cdot 4\pi M) \cdot (H - (1 + P)2\pi M)}. \quad \text{(A3b)}$$

With these formulas and for the same value of the packing density $P = 0.26$, we find that taking into account DDI does not lead to any improvement in fitting experimental results, similar to the case of the in-plane sample magnetization.

---

[1] K. Sakoda, *Optical Properties of Photonic Crystals* (Springer, Berlin, 2001).

[2] E. Istrate and E. H. Sargent, Rev. Mod. Phys. **78**, 455 (2006).

[3] A. I. Akhiezer, V. G. Baryakhtar, and S. V. Peletminskii, *Spin-Waves* (North-Holland, Amsterdam, 1968).

[4] V. V. Kruglyak, S. O. Demokritov, and D. Grundler, J. Phys. D **43**, 264001 (2010).

[5] M. P. Kostylev, A. A. Stashkevich, and N. A. Sergeeva, Phys. Rev. B **69**, 064408 (2004).

[6] M. Krawczyk and H. Puszkarski, Phys. Rev. B **77**, 054437 (2008).

[7] J. Jorzick, S. O. Demokritov, B. Hillebrands, B. Bartenlian, C. Chappert, D. Decannini, F. Rousseaux, and E. Cambril, Appl. Phys. Lett. **75**, 3859 (1999).

[8] J. Jorzick, C. Kramer, S. O. Demokritov, B. Hillebrands, E. Sondergard, M. Bailleul, C. Fermon, U. Memmert, A. N. Muller, A. Kounga, U. Hartmann, and E. Tsymbal, J. Magn. Magn. Mater. **226**, 1835 (2001).

[9] Z. K. Wang, V. L. Zhang, H. S. Lim, S. C. Ng, M. H. Kuok, S. Jain, and A. O. Adeyeye, Appl. Phys. Lett. **94**, 083112 (2009).

[10] J. Ding, M. Kostylev, and A. O. Adeyeye, Phys. Rev. Lett. **107**, 047205 (2011).

[11] S. Neusser and D. Grundler, Adv. Mater. **21**, 2927 (2009).

[12] V. V. Kruglyak, P. S. Keatley, A. Neudert, R. J. Hicken, J. R. Childress, and J. A. Katine, Phys. Rev. Lett. **104**, 027201 (2010).

[13] K.-S. Lee, D.-S. Han, and S.-K. Kim, Phys. Rev. Lett. **102**, 127202 (2009).

[14] G. Gubbiotti, S. Tacchi, G. Carlotti, P. Vavassori, N. Singh, S. Goolaup, A. O. Adeyeye, A. Stashkevich, and M. Kostylev, Phys. Rev. B **72**, 224413 (2005).

[15] S. A. Nikitov, Ph. Tailhades, and C. S. Tsai, J. Magn. Magn. Mater. **236**, 320 (2001).

[16] A. V. Chumak, A. A. Serga, S. Wolf, B. Hillebrands, and M. P. Kostylev, Appl. Phys. Lett. **94**, 172511 (2009).

[17] S. Tacchi, M. Madami, G. Gubbiotti, G. Carlotti, H. Tanigawa, T. Ono, and M. P. Kostylev, Phys. Rev. B **82**, 024401 (2010).

[18] V. G. Golubev, in *Advanced Materials and Technologies for Micro/Nano-Devices, Sensors and Actuators*, edited by E. Gusev *et al.* (Springer Science + Business Media B. V., Dordrecht, the Netherlands, 2010), p. 101.

[19] S. M. Weekes, F. Y. Ogrin, W. A. Murray, and P. S. Keatley, Langmuir **23**, 1057 (2007).

[20] M. Kostylev, R. Magaraggia, F. Y. Ogrin, E. Sirotkin, V. F. Mescheryakov, N. Ross, and R. L. Stamps, IEEE Trans. Magn. **44**, 2741 (2008).

[21] N. Ross, M. Kostylev, and R. L. Stamps, J. Appl. Phys. **109**, 013906 (2011).

[22] K. S. Napolskii, A. Sinitskii, S. V. Grigoriev, N. A. Grigorieva, H. Eckerlebe, A. A. Eliseev, A. V. Lukashin, and Y. D. Tretyakov, Physica B **397**, 23 (2007).

[23] N. Sapoletova, T. Makarevich, K. Napolskii, E. Mishina, A. Eliseev, A. van Etteger, T. Rasing, and G. Tsirlina, Phys. Chem. Chem. Phys. **12**, 15414 (2010).

[24] S. V. Grigoriev, K. S. Napolskii, N. A. Grigoryeva, A. V. Vasilieva, A. A. Mistonov, D. Y. Chernyshov, A. V. Petukhov, D. V. Belov, A. A. Eliseev, A. V. Lukashin, Yu. D. Tretyakov, A. S. Sinitskii, and H. Eckerlebe, Phys. Rev. B **79**, 045123 (2009).

[25] K. S. Napolskii, N. A. Sapoletova, D. F. Gorozhankin, A. A. Eliseev, A. V. Petukhov, D. V. Byelov, A. A. Mistonov, N. A. Grigoryeva,

W. G. Bouwman, K. O. Kvashnina, A. A. Snigirev, D. Yu. Chernyshov, A. V. Vassilieva, and S. V. Grigoriev, Langmuir **26**, 2346 (PS) (2010).

[26] A. Sinitskii, V. Abramova, N. Grigorieva, S. Grigoriev, A. Snigirev, D. V. Belov, and A. V. Petukhov, Europhys. Lett. **89**, 14002 (2010).

[27] V. V. Abramova, A. S. Sinitskii, N. A. Grigor'eva, S. V. Grigor'ev, D. V. Belov, A. V. Petukhov, A. A. Mistonov, A. V. Vasil'eva, and Yu. D. Tret'yakov, J. Exp. Theor. Phys. **109**, 29 (2009).

[28] M. Borsboom, W. Bras, I. Cerjak, D. Detollenaere, D. G. van Loon, P. Goedtkindt, M. Konijnenburg, P. Lassing, Y. K. Levine, B. Munneke, M. Oversluizen, R. van Tol, and E. Vlieg, J. Synchrotron Radiat. **5**, 518 (1998).

[29] W. Bras, I. P. Dolbnya, D. Detollenaere, R. van Tol, M. Malfois, G. N. Greaves, A. J. Ryan, and E. Heeley, J. Appl. Crystallogr. **36**, 791 (2003).

[30] S. Nikitenko, A. M. Beale, A. M. J. van der Eerden, S. D. M. Jacques, O. Leynaud, M. G. O'Brien, D. Detollenaere, R. Kaptein, B. M. Weckhuysen, and W. Bras, J. Synchrotron Radiat. **15**, 632. (2008).

[31] A. Snigirev, V. Kohn, I. Snigireva, and B. Lengeler, Nature **384**, 49 (1996).

[32] S. Förster, A. Timmann, C. Schellbach, A. Frömsdorf, A. Kornowski, H. Weller, S. V. Roth, and P. Lindner, Nat. Mater. **6**, 888 (2007).

[33] Kittel C., *Introduction to Solid State Physics*, 7th ed. (Wiley, New York, 1996).

[34] L. Woodcock, Nature **385**, 141 (1997).

[35] J. V. Sanders, Nature **204**, 1151 (1964).

[36] H. Miguez, F. Meseguer, C. Lopez, A. Mifsud, J. C. Moya, and L. Vazkuez, Langmuir **13**, 6009 (1997).

[37] P. N. Pusey, W. van Megen, P. Bartlett, B. J. Ackerson, J. G. Rarity, and S. M. Underwood, Phys. Rev. Lett. **63**, 2753 (1989).

[38] Y. A. Vlasov, V. N. Astratov, A. V. Baryshev, A. A. Kaplyanskii, O. Z. Karimov, and M. F. Limonov, Phys. Rev. E **61**, 5784 (2000).

[39] J. Hilhorst, V. V. Abramova, A. Sinitskii, N. A. Sapoletova, K. S. Napolskii, A. A. Eliseev, D. V. Byelov, N. A. Grigoryeva, A. V. Vasilieva, W. G. Bouwman, K. Kvashnina, A. Snigirev, S. V. Grigoriev, and A. V. Petukhov, Langmuir **25**, 10408 (2009).

[40] A. A. Eliseev, D. F. Gorozhankin, K. S. Napolskii, A. V. Petukhov, N. A. Sapoletova, A. V. Vasilieva, N. A. Grigoryeva, A. A. Mistonov, D. V. Byelov, W. G. Bouwman, K. O. Kvashnina, D. Yu. Chernyshov, A. A. Bosak, and S. V. Grigoriev, JETP Lett. **90**, 272 (2009).

[41] C. Bilzer, T. Devolder, P. Crozat, and C. Chappert, J. Appl. Phys. **101**, 074505 (2007).

[42] M. Weiler, A. Brandlmaier, S. Geprägs, M. Althammer, M. Opel, C. Bihler, H. Huebl, M. S. Brandt, R. Gross, and S. T. B. Goennenwein, New J. Phys. **11**, 013021 (2009).

[43] J. Jorzick, S. O. Demokritov, B. Hillebrands, D. Berkov, N. L. Gorn, K. Guslienko, and A. N. Slavin, Phys. Rev. Lett. **88**, 047204 (2002).

[44] E. H. Frei, S. Shtrikman, and D. Treves, Phys. Rev. **106**, 446 (1957).

[45] E. C. Stoner and E. P. Wohlfarth, Philos. Trans. R. Soc. A **240**, 599 (1948).

[46] E. P. Wohlfarth, J. Appl. Phys., Suppl. **30**, 117, (1960).

[47] G. Gubbiotti, S. Tacchi, M. Madami, G. Carlotti, A. O. Adeyeye, and M. Kostylev, J. Phys. D **43**, 264003 (2010).

[48] E. V. Tartakovskaya, J. Magn. Magn. Mater. **322**, 3495 (2010).

[49] A. Encinas-Oropesa, M. Demand, L. Piraux, I. Huynen, and U. Ebels, Phys. Rev. B **63**, 104415 (2001).

[50] A. A. Stashkevich, Y. Roussigné, P. Djemia, S. M. Chérif, P. R. Evans, A. P. Murphy, W. R. Hendren, R. Atkinson, R. J. Pollard, A. V. Zayats, G. Chaboussant, and F. Ott, Phys. Rev. B **80**, 144406 (2009).

[51] S. Jain, M. P. Kostylev, and A. O. Adeyeye, Phys. Rev. B **82**, 214422 (2010).

[52] J. Ding, M. Kostylev, and A. O. Adeyeye, Phys. Rev. B **84**, 054425 (2011).

[53] C. S. Chang, M. Kostylev, A. O. Adeyeye, M. Bailleul, and S. Samarin, Europhys. Lett. **96**, 57007 (2011).

[54] R. Magaraggia, M. Hambe, M. Kostylev, V. Nagarajan, and R. L. Stamps, Phys. Rev. B **84**, 104441 (2011).

[55] A. G. Gurevich and G. A. Melkov, *Magnetization Oscillations and Waves* (CRC Press, New York, 1996).

[56] E. V. Tartakovskaya, Phys. Rev. B **71**, 180404(R) (2005).

[57] J. D. Jackson, *Classical Electrodynamics* (Wiley, New York, 1975).

[58] Z. K. Wang, M. H. Kuok, S. C. Ng, D. J. Lockwood, M. G. Cottam, K. Nielsch, R. B. Wehrspohn, and U. Gösele, Phys. Rev. Lett. **89**, 027201 (2002).